Weakly anisotropic residual contact stress in silicon demonstrated by electron backscatter diffraction and expanding cavity models

Robert F. Cook, and Lawrence H. Friedman

Articles you may be interested in

Weakly anisotropic residual contact stress in silicon demonstrated by electron backscatter diffraction and expanding cavity models

Robert F. Cook[a)] and Lawrence H. Friedman

Materials Measurement Science Division, National Institute of Standards and Technology, Gaithersburg, Maryland 20899, USA

The residual stress field surrounding an elastic-plastic spherical indentation contact in Si is determined by electron backscatter diffraction (EBSD)-based experimental measurements and expanding hemispherical cavity-based models. The experiments provide support for indentations as test vehicles for assessment of EBSD as a two-dimensional deformation mapping method but make clear that selection of coordinate axes is critical to determining the correct representation of a stress field. The use of principal stress coordinates rather than the conventional Cartesian coordinates is required in cases in which the direction of the stress field is not aligned with Cartesian axes. In particular, the use of principal coordinates in the analysis of a spherical indentation stress field in Si removed misleading artefacts from the Cartesian-based field and revealed only a weak effect of Si crystalline elastic anisotropy. The experimental results are supported by isotropic and anisotropic finite element analysis models. https://doi.org/10.1063/1.5055859

Small-scale measurement and mapping of stress and strain are critical to the design, manufacturing, and operation of many advanced devices, especially load-bearing components (e.g., beams, axles) in microelectromechanical systems (MEMS) and at thermal expansion mismatched (e.g., metal-insulator) interfaces in microelectronic components. In particular, stress distributions adjacent to grain boundary grooves in polycrystals, localized contacts on surfaces, and sharp corners at internal edges significantly affect the strengths of MEMS components,[1] thereby limiting manufacturing yield, operational reliability, and innovation in design. Recent work has demonstrated the applicability of electron backscatter diffraction (EBSD) to measuring stress and strain with sub-micrometer resolution in materials frequently used in MEMS and microelectronics, including silicon (Si),[2–9] germanium (Ge),[10] SiGe,[2,11–14] and barium titanate ($BaTiO_3$).[15,16] In some cases, measurements have been presented as one-dimensional (1-D) line scans across 1-D structures such as patterned lines, wedge contacts, or elongated domains.[3–5,10–12,14–16] In other cases, measurements have been presented as two-dimensional (2-D) maps of these and other 2-D, structures, such as pyramidal or spherical indentations, tensile bars, or thin films.[6–9,12,15,16] In all cases, the line scans or maps have presented components of the stress, strain, or rotation tensors in Cartesian coordinates. In most cases, such coordinates provide a clear representation of the deformation field, as the coordinates are aligned with a structural feature of interest (e.g., along a wedge contact[5]). In some cases, however, Cartesian coordinates provide misleading representations of the field, obscuring the fundamental physics of structural deformation and impeding an assessment of the effects of material elastic anisotropy. This is the case for indentation contacts in Si.[6–8]

Indentations are of importance as test vehicles in the assessment of multi-axial deformation states, as quantitative elements in predicting MEMS component strength, and in providing insights into the fundamental nature of contact fields. It is therefore important to have a correct representation of the indentation deformation field. This Letter extends a previous work[8] to examine the effects of the coordinate system and elastic anisotropy on the 2-D stress field determined by EBSD adjacent to an elastic-plastic spherical indentation in Si. The experimental measurements provide context for examination of the ability of a spherical expanding cavity model to describe the stress field.

The experimental indentation and EBSD strain measurement methods are described in detail elsewhere.[8] Briefly, a circular residual indentation impression, about 4 μm in diameter and 200 nm in depth, was formed on the (001) surface of a single crystal Si disc using a conospherical diamond probe of 5 μm radius at a peak load of 200 mN. The residual deformation field consisted of indentation-localized plastic deformation, largely restricted to a zone beneath the impression, and extended elastic deformation, including surface uplift, surrounding the zone and impression. The mean supported contact stress, the hardness, of Si during such elastic-plastic indentations is about 10 GPa.[1] The peak load was selected to be small enough, so that no indentation cracks were generated to potentially perturb the deformation field. The theoretical strength of Si is about 20 GPa and MEMS devices typically exhibit about 3 GPa strength.[1] Electron backscatter patterns (EBSPs) were obtained in a 128 × 128 grid over a 48 μm × 48 μm region surrounding the impression. An EBSP obtained far from the impression was selected as a reference and other EBSPs were compared with the reference using cross-correlation techniques to obtain the deformation field in terms of the displacement gradient tensor, A_{ij}, at each grid location. A_{ij} was separated into symmetric, ε_{ij}, and anti-symmetric, ω_{ij}, components, interpreted as infinitesimal strain and rotation tensors, respectively. The coordinate system $(i, j) = (1, 2, 3)$ in the laboratory frame was taken as a Cartesian set related to the crystallographic frame by $(1, 2, 3) = ([110], [1\bar{1}0], [001])$. Full depictions of ε_{ij} and ω_{ij} are given in the supplementary material for 10 μm × 10 μm

a)Author to whom correspondence should be addressed: robert.cook@nist.gov

regions encompassing the impression and are similar to those given previously for Vickers indentation.[6,7]

Figure 1 shows $10\,\mu m \times 10\,\mu m$ color-filled contour maps of the σ_{11}, σ_{12}, and σ_{22} components of the stress tensor in the above [110]-based laboratory frame. The stress and strain tensors in the crystallographic frame (denoted σ_{ij}^* and ε_{ij}^*) are related by $\sigma_{ij}^* = c_{ijkl}\varepsilon_{kl}^*$, where c_{ijkl} is the elastic stiffness tensor in the crystallographic frame, and the Einstein summation convention is used. In cubic Si, the only non-zero elastic stiffness components in the crystallographic frame are $c_{11} = 167.4\,GPa$, $c_{12} = 65.2\,GPa$, and $c_{44} = 79.6\,GPa$,[17] using the Voigt contracted matrix notation. Stresses in the crystallographic and laboratory frames are related by a simple rotation transformation. The EBSD technique assumes that the surface is free of normal traction,[10] $\sigma_{33} = 0$, and, experimentally, the other traction components are also negligible, $\sigma_{13} \approx \sigma_{23} \approx 0$. The gray discs in Fig. 1 cover the contact impression from which no stress information was obtained. Some expected features of these indentation maps include: that stress values remote from the indentation are not sufficient to cause plastic deformation or fracture; that there are dominant lobes of negative stress associated with the compressive effects of forming the indentation impression in the surface; and the extent of the lobes to about three indentation diameters.[18] An additional clear feature of the maps of Fig. 1 is that all stress tensor components exhibited lobes of positive and negative values and two-fold symmetry—features in common with previous maps of strain tensors about indentations[6–8] (see supplementary material) and superficially at variance with the four-fold elastic symmetry of the [001] axis and Raman spectroscopy-based maps of stress[8] [rotation tensor components exhibited four-fold symmetry and mirror planes[6,7] (SM)]. Use of crystallographic [100]-[010]-[001] coordinates rotates and alters the shape of the lobes, but does not alter the symmetry of the stress or strain maps. The lobes of Fig. 1 and elsewhere give a somewhat misleading impression of the nature of the indentation stress field and the influence of the elastic anisotropy of Si. Specifically, as exemplified in Fig. 1 and earlier,[6–8] (SM) the lobes of the normal stress or strain components are aligned with the (1, 2) coordinate axes used and the lobes of the shear components are rotated $\pi/4\,rad$ about the 3-axis from the (1, 2) axes.

The origin of the indentation stress field and the effects of elastic anisotropy were further investigated by developing a finite element analysis (FEA) model of the indentation plastic deformation zone and the surrounding elastically deformed material. The plastic zone was modeled as an expanding cavity-like hemisphere[18] of $4\,\mu m$ initial diameter imbedded in the (001) Si surface, with hydrostatic initial strain, $\varepsilon_{11} = \varepsilon_{22} = \varepsilon_{33} = 0.03$. Two material models were implemented: the first material model was elastically isotropic Si using a Reuss-average isotropic Young's modulus of $E = 159\,GPa$ and a Poisson's ratio of $\nu = 0.23$;[19] the second material model assumed elastically anisotropic Si using the same stiffnesses c_{IJ} given above. FEA was performed with Abaqus.[20,21] Elastic behavior incorporated geometric nonlinearity via logarithmic ("true") strains, but did not incorporate material nonlinearity. The modeled volume spanned $200\,\mu m$, much larger than the span of the stressed area surrounding the indentation, about $20\,\mu m$, and the indentation contact, $4\,\mu m$. The mesh consisted of $557\,000$ quadratic tetrahedral (C3D10) elements arranged in an adapted mesh. When compared with a coarser mesh of $214\,000$ elements, the relative root-mean-square stress difference was less than 1%. Stress components were calculated in material cubic coordinates and converted to laboratory coordinates for comparison with experimental data.

Figure 2 shows maps of the σ_{11}, σ_{12}, and σ_{22} components of the stress tensor determined from the isotropic FEA model using the same spatial and stress scales as Fig. 1. Comparing the two figures, the similarity of the shapes, orientations, and scales of the stress lobes is striking, suggesting
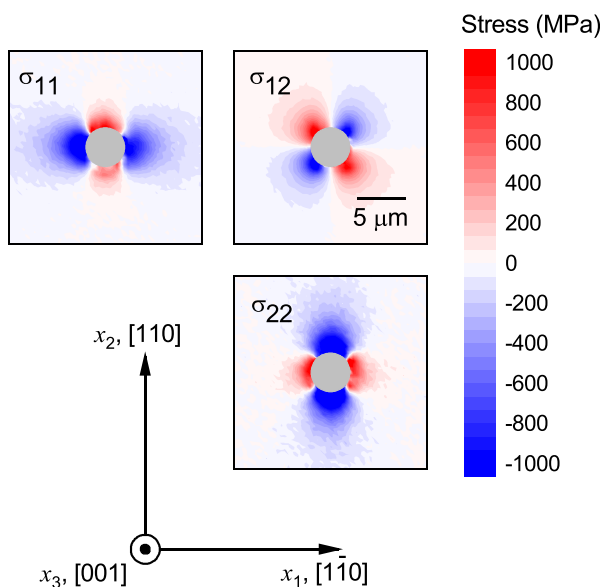

FIG. 1. Experimental EBSD measurements represented as color-filled contour maps of the major stress components surrounding a spherical indentation in (001) Si.
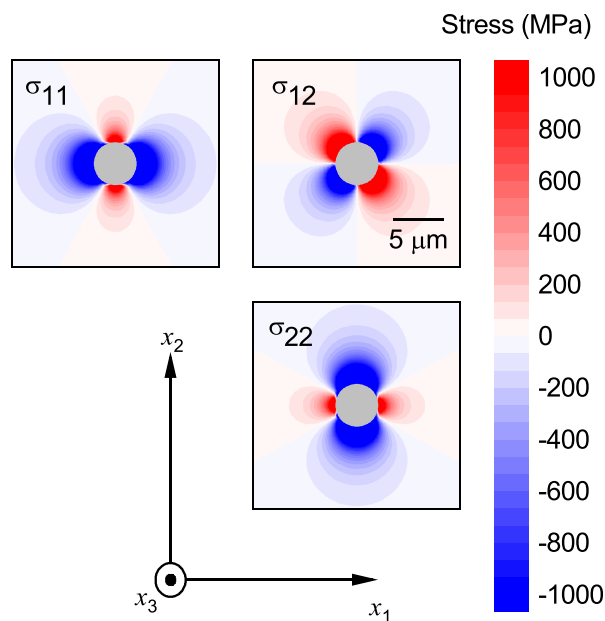

FIG. 2. FEA modeling represented as color-filled contour maps of the major stress components surrounding a spherical indentation represented by a hemispherical expanding cavity imbedded in an isotropic solid.

three conclusions: (i) the magnitudes of the imposed initial strains and the hemispherical size and shape were appropriate representations of the plastic deformation zone (and comparable to previous similar models and observations[5,7,22]); (ii) to first approximation, the residual stress field surrounding an indentation in Si is described by a zone of hemispherical expansion imbedded in an isotropic medium; and (iii) the lobes of stress cannot be related to elastic symmetry of the indented isotropic material, but related to the choice of coordinate axes. Figure 3 shows the same stress components determined from the anisotropic FEA model and reinforces these conclusions. The major lobes of stress are slightly elongated relative to those determined from the isotropic model (Fig. 2) and a better representation of the experimental observations (Fig. 1), but the similarities of shape, orientation and scale of Figs. 1 and 3 are clear. In these cases, the two-fold symmetric lobes of stress cannot be related to the elastic symmetry of the indented anisotropic material as the [001] indentation axis is four-fold rotationally elastically symmetric.

An unbiased assessment of the stress state can be made using the minimum and maximum principal stress components,[23] shown in Fig. 4 using the same scales as Figs. 1–3. Figures 4(a) and 4(b) show the principal stress components resulting from the isotropic FEA model. The minimum principal stress, Fig. 4(a), is completely compressive and the maximum principal stress, Fig. 4(b), is completely tensile. As anticipated for an isotropic material, the magnitudes of the principal components exhibit no angular dependence and the contours are concentric circles: those of the maximum principal stress are slightly smaller in diameter. The maximum principal stress directions (not shown) also form concentric circles [similar to Figs. 4(a) and 4(b)]. Figures 4(c) and 4(d) show the minimum and maximum principal stress components, respectively, resulting from the anisotropic FEA model. As in the isotropic case, the minimum and
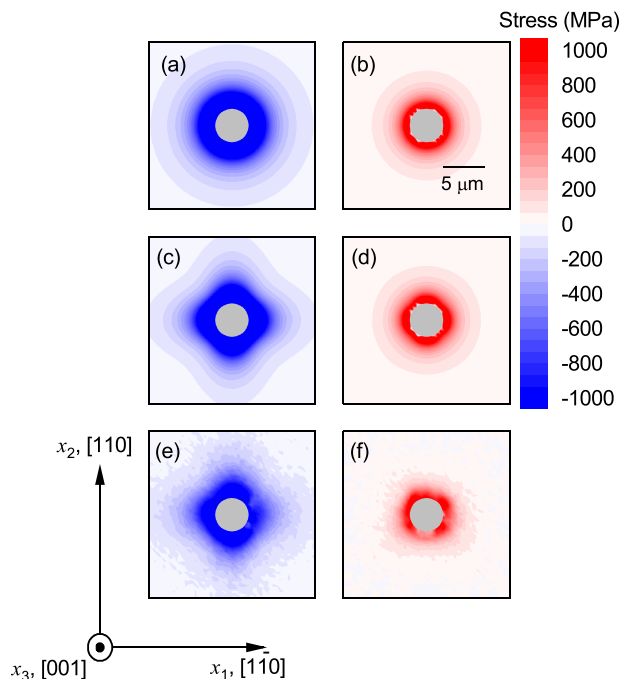

FIG. 4. Color-filled contour maps of the principal stress components surrounding a spherical indentation: (a) and (b) determined by modeling an isotropic solid, Fig. 2; (c) and (d) determined by modeling anisotropic Si, Fig. 3; and (e) and (f) determined by experimental EBSD measurements, Fig. 1.

maximum principal stresses are also completely compressive or tensile. In this case, however, the magnitude of the minimum principal stress exhibits angular anisotropy, forming a rounded diamond shape, Fig. 4(c). The magnitude of the maximum principal stress again exhibits essentially no apparent angular anisotropy, Fig. 4(d), forming near circles. Also, again, the directions of the maximum principal stress form near circles. Figures 4(e) and 4(f) show the magnitudes of the principal stresses determined from the experimental stress measurements (Fig. 1). The minimum and maximum principal stresses are completely compressive and tensile, respectively, and the magnitudes of the minimum and maximum principal stresses form rounded diamond shapes and circles, respectively. The circles of maximum principal stress are somewhat smaller than the diamonds of minimum principal stress. The similarity of the anisotropic model results, Figs. 4(c) and 4(d), and the experimental measurements, Figs. 4(e) and 4(f), is clear. In particular, the four-fold elastic symmetry of the system is indicated in the minimum principal stress rounded diamond contours. The maximum principal stress directions are weakly perturbed circles: the majority of the principal stress directions in the experiment and the anisotropic model were within ±4° of those of the isotropic model.

A somewhat unbiased assessment of the stress state can also be made using the radial and circumferential components of cylindrical polar coordinates, although an axis of rotation—the center of the indentation—must be selected. Using cylindrical polar coordinates here resulted in maps (not shown) almost identical to those of Figs. 1 and 4(e) and 4(f), consistent with the almost complete separation of radial compression and circumferential tension about the indentation impression. Using a "traceless" initial strain tensor to represent an ideally plastic indentation process within the
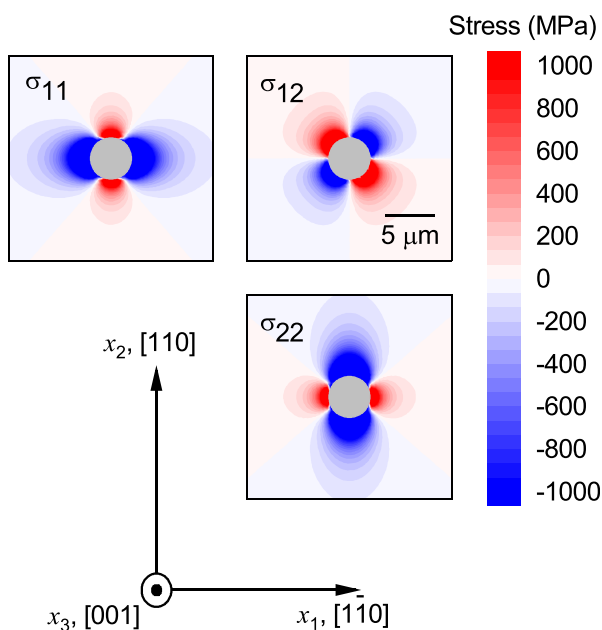

FIG. 3. FEA modeling represented as color-filled contour maps of the major stress components surrounding a spherical indentation in (001) Si represented by an imbedded hemispherical expanding cavity. Compare with Fig. 1.

hemispherical zone, such that $\varepsilon_{33} = -2\varepsilon_{11} = -2\varepsilon_{22}$, resulted in maps almost identical to Figs. 3 and 4(c) and 4(d), suggesting that the residual stress field results almost entirely from radial expansion and is little affected by axial effects normal to the free surface. Using a greater hydrostatic initial strain of $\varepsilon_{11} = \varepsilon_{22} = \varepsilon_{33} = 0.05$ resulted in the enlargement of all the modelled stress contours, such that the agreements between Figs. 1, 3, and 4 were removed, suggesting that a detailed comparison of the model and the experiment could be used to infer the extent of plastic deformation in the zone.

A key point in the work here, not to be overlooked in considerations of anisotropy, is that Figs. 4(e) and 4(f) provide direct experimental evidence of the residual stress field exterior to an elastic-plastic contact impression. A sub-point is that in order to generate a residual stress field, the contact need not be "sharp" in the sense of contact acuity, so long as the strain imposed by the contact is at least partially accommodated in the material by localized plastic deformation. This was the case here: a spherical contact was deep enough to generate a plastic deformation zone in Si. The importance of residual stress fields is that they act to initiate and propagate cracks from nascent defects generated in the plastic zone. Transmission electron microscopy can identify such defects.[22] However, EBSD, as used here (or Raman spectroscopy[8]), is required to quantify the residual (tensile) stress field, and fracture mechanics can then be used to make predictions of the strength of MEMS[1] and other devices. The FEA model used here and earlier[5] treated the plastic deformation zone as a region of homogeneous initial strain. EBSD measurements can be used to calibrate this strain (here 0.03) and the model then extended to predictions of crack *propagation* adjacent to contacts of varying geometry. A model for indentation crack *initiation*, however, requires explicit consideration of inhomogeneous strain and defect generation beneath the contact, such as a cohesive-zone-based FEA model applied earlier in consideration of cracking and strain at a Vickers indentation.[7]

Finally, the observations here, represented in principal rather than Cartesian coordinates, make clear that the residual stress field associated with [001] spherical indentation in Si is four-fold rotationally symmetric, consistent with Si crystallography. The symmetry is most clearly observed in the minimum (compressive) principal stress that exhibits maxima in the $\langle 110 \rangle$ directions, along the directions of the chains of Si atoms in the structure and hence directions of the greatest resistance to elastic deformation. Conversely, the elastic anisotropy is only weakly observed, if at all, in the maximum (tensile) principal stress that exhibits a near circular symmetry. An important conclusion thus is that the significant tendency to $\langle 110 \rangle$ indentation cracking (surface traces aligned with image edges in Fig. 4) for [001] indentations reflects the smaller fracture surface energy for $\{110\}$

planes relative to other planes in the [001] zone and fewer bonds perpendicular to the chains of atoms[1] rather than stress field anisotropy. Although Raman spectroscopy-based stress field maps, which are determined by the entire stress or strain tensor,[24,25] can also reflect the symmetry of the material,[8] principal stress analysis is still required to obtain unambiguous driving forces for deformation and fracture.

See supplementary material for "raw" strain and rotation data in laboratory Cartesian coordinates as the basis for stress analysis in principal coordinates.

[1]F. W. DelRio, R. F. Cook, and B. L. Boyce, Appl. Phys. Rev. **2**, 021303 (2015).

[2]S. Villert, C. Maurice, C. Wyon, and R. Fortunier, J. Microsc. **233**, 290 (2009).

[3]M. D. Vaudin, Y. B. Gerbig, S. J. Stranick, and R. F. Cook, Appl. Phys. Lett. **93**, 193116 (2008).

[4]M. D. Vaudin, G. Stan, Y. B. Gerbig, and R. F. Cook, Ultramicroscopy **111**, 1206 (2011).

[5]L. H. Friedman, M. D. Vaudin, S. J. Stranick, G. Stan, Y. B. Gerbig, W. A. Osborn, and R. F. Cook, Ultramicroscopy **163**, 75 (2016).

[6]A. J. Wilkinson and T. B. Britton, Mater. Today **15**, 366 (2012).

[7]T. B. Britton, J. Jiang, R. Clough, E. Tarleton, A. I. Kirkland, and A. J. Wilkinson, Ultramicroscopy **135**, 136 (2013).

[8]A. J. Gayle, L. H. Friedman, R. Beams, B. G. Bush, Y. B. Gerbig, C. A. Michaels, M. D. Vaudin, and R. F. Cook, J. Appl. Phys. **122**, 205101 (2017).

[9]M. J. McLean and W. A. Osborn, Ultramicroscopy **185**, 21 (2018).

[10]A. J. Wilkinson, G. Meaden, and D. J. Dingley, Ultramicroscopy **106**, 307 (2006).

[11]A. J. Wilkinson, Appl. Phys. Lett. **89**, 241910 (2006).

[12]A. J. Wilkinson, G. Meaden, and D. J. Dingley, Superlattices Microstruct. **45**, 285 (2009).

[13]M. D. Vaudin, W. A. Osborn, L. H. Friedman, J. M. Gorham, and R. F. Cook, Ultramicroscopy **148**, 94 (2015).

[14]W. A. Osborn, L. H. Friedman, and M. D. Vaudin, Ultramicroscopy **184**, 88 (2018).

[15]J. A. Howell, M. D. Vaudin, and R. F. Cook, J. Mater. Sci. **49**, 2213 (2014).

[16]J. A. Howell, M. D. Vaudin, L. H. Friedman, and R. F. Cook, J. Mater. Sci. **52**, 12608 (2017).

[17]H. J. McSkimin, W. L. Bond, E. Buehler, and G. K. Teal, Phys. Rev. **83**, 1080 (1951).

[18]K. L. Johnson, *Contact Mechanics* (Cambridge University Press, Cambridge, United Kingdom, 1996).

[19]J. P. Hirth and J. Lothe, *Theory of Dislocations*, 2nd ed. (Krieger Publishing, Malabar, Florida, 1982, reprinted 1992).

[20]Abaqus v.6.14-5, Dassault Systèmes Simulia Corp. Providence, RI, 2014.

[21]Certain commercial software is identified to specify the numerical study adequately. This does not imply endorsement by NIST or that the software is the best available for the purpose.

[22]J. E. Bradby, J. S. Williams, J. Wong-Leung, M. V. Swain, and P. Munroe, J. Mater. Res. **16**, 1500 (2001).

[23]G. E. Mase, *Continuum Mechanics* (McGraw-Hill, New York, 1970).

[24]Q. Ma, S. Chiras, D. R. Clarke, and Z. Suo, J. Appl. Phys. **78**, 1614 (1995).

[25]R. P. Koseski, W. A. Osborn, S. J. Stranick, F. W. DelRio, M. D. Vaudin, T. Dao, V. H. Adams, and R. F. Cook, J. Appl. Phys. **110**, 073517 (2011).